Comparison of a Lattice Boltzmann Simulation of Steep Internal Waves and Laboratory Measurements using Particle Image Velocimetry

J. M. Buick[1†], A. J. Martin[2], J. A. Cosgrove[1], C. A. Greated[1] and W. J. Easson[2]

[1] Department of Physics and Astronomy The University of Edinburgh

The Kings Buildings, Mayfield Road

Edinburgh EH9 3JZ, Scotland UK.

[2] School of Mechanical Engineering at the University of Edinburgh

Sanderson Building, The King's Buildings

Edinburgh, EH9 3JL, Scotland, UK.

† J.M.Buick@ed.ac.uk, tel: 0131 6505259, fax: 0131 6505212.

July 9, 2002

Abstract

Progressive interfacial waves are simulated between two viscous, immiscible fluids using a lattice Boltzmann model and compared to waves generated in a laboratory tank, where their velocities are measured using a film-based particle image velocimetry system. The numerical and experimental velocities are compared for two similar, steep waves and the results are found to be in good agreement. The results are also compared with a first order wave theory, in both cases they predict velocities up to 40% greater than the theory.

Keywords: Internal waves; lattice Boltzmann; particle image velocimetry; non-linear waves; gravity waves.

1 Introduction

Interfacial internal waves occur between fluids with different densities, such as when fresh water flows onto salt water in an estuary, or where there is a sharp increase in a fluid's potential density with depth, such as at a sharp thermoclyne in the ocean. The stratification conditions required to sustain internal wave motion are present in many bodies of water including all of the deep oceans, and there are many mechanisms which can generate the waves.

The vertical excursions made by fluids elements during the passage of an in-

ternal wave is likely to be much greater than that of surface waves, even if both are forced by the same event, such as an earthquake, wind shear or tidal forcing. Such internal wave motion, be it a regular or occasional occurrence, can have an important influence on offshore operations [1, 2]. In most cases surface waves, currents and wind loading will be dominant in determining the design of an offshore drilling platforms, however, the design of risers and mooring lines may be significantly influenced by internal waves. One area where there is at present drilling interest is the United Kingdom North-West Approaches. This is a region between Shetland, the Faeroe Islands and the north of mainland Scotland. Relatively warm water is driven through this area by the North Atlantic Drift which flows above a region of colder water known as Norwegian Deep Water. In this region there is evidence of internal waves [3]. In such circumstances an understanding of the wave kinematics is clearly important.

Recent developments in the study of this phenomenon have included numerical simulations using a lattice Boltzmann (LB) model [4] and the measurement of whole two-dimensional velocity fields using Particle Image Velocimetry (PIV) [5]. Here we consider both of these techniques and make a comparison between the velocities obtained for two similar waves.

Other theoretical and numerical methods [6, 7, 8, 9, 10] are available which can be applied to study internal waves. Unlike many numerical schemes which

consider an inviscid fluid the LB model incorporates the correct viscous behaviour of the fluids. The alternative approach to numerical modelling which is offered by the LB model could offer advantages in a number of areas. For example, the LB model has been shown to be ideal for simulating complex or irregular boundaries. This suggests that the LB technique would be useful for studying problems involving the interaction of internal waves with sills and complex bed topography. The nature of the LB model makes it ideally suited to parallel implementation, enabling efficient use of ever expanding computer resources.

2 Lattice Boltzmann simulations of interfacial waves

The LB technique [11, 12] involves simulating the Boltzmann equation,

$$f_i(\boldsymbol{r}+\boldsymbol{e}_i, t+1) - f_i(\boldsymbol{r}, t) = \frac{-1}{\tau}[f_i(\boldsymbol{r}, t) - \overline{f}_i(\boldsymbol{r}, t)], \text{for} \quad i = 0, 1, ..., b, \quad (1)$$

on a regular grid where each grid point is connected to b neighbours by the vectors $\boldsymbol{e}_i$ for i = 1, 2, ..., b and where $\boldsymbol{e}_0$ is the null vector. Here $f_i(\boldsymbol{r}, t)$ is the distribution function of the ith link at site $\boldsymbol{r}$ and time t. The equilibrium value of the distribution function, $\overline{f}_i$, is defined so that the simulated fluid has the correct macroscopic properties and the relaxation time, τ, is a free variable which determines the fluid viscosity. The form of $\overline{f}_i$ used in this study and

the macroscopic equations which it satisfies will be considered below. The fluid density and momentum are defined at each site and each time step as

$$\rho = \sum_{i=0}^{b} f_i \tag{2}$$

and

$$\rho \boldsymbol{u}_i = \sum_{i=0}^{b} f_i \boldsymbol{e}_i. \tag{3}$$

The simulation is completely discretized in space and time and is ideally suited to parallel implementation.

Here we employ a binary fluid model [13, 14] which simulates two immiscible fluids which, in the presence of gravity [15, 4], can have different potential densities. This LB approach to interfacial wave simulation has been developed from the lattice gas model which has previously been used to simulate surface waves [16, 17]. It has been applied successfully to linear, internal standing waves and the results compared favorably with theory in a previous paper, [4], where the model is described in detail. Here we give a brief description of the numerical technique. The simulations are performed on a hexagonal grid ($b = 6$) with the unit link vectors given by $\boldsymbol{e}_i = \sin(\frac{\pi i}{3} - \frac{\pi}{6})\boldsymbol{i} + \cos(\frac{\pi i}{3} - \frac{\pi}{6})\boldsymbol{k}$, for $i = 1, 2, ..., 6$, where $\boldsymbol{i}$ and $\boldsymbol{k}$ are orthogonal unit vectors in the horizontal and vertical directions respectively. The system is described in terms of the overall density (irrespective

of fluid type), ρ, and the density difference, $\Delta\rho$, between the two fluids. Thus, if the two fluids we are considering have densities ρ_1 and ρ_2, then $\rho = \rho_1 + \rho_2$ and $\Delta\rho = \rho_1 - \rho_2$ so that $\Delta\rho$ will be constant in each fluid (other than a small density change in each fluid introduced by the gravitational force) and positive in one fluid and negative in the other; in the interface region $\Delta\rho$ varies smoothly through zero with a tanh-like profile. The values of ρ and $\Delta\rho$ are found from the distribution functions f_i and d_i as $\rho = \sum_i f_i$ and $\Delta\rho = \sum_i d_i$ while the fluid velocity, $\boldsymbol{u}$, is given by $\rho\boldsymbol{u} = \sum_i f_i \boldsymbol{e}_i$. The two distribution functions are simulated directly using two Boltzmann equations. The first one describes the motion of the entire system and is the same as equation (1) with an additional gravity term:

$$f_i(\boldsymbol{r} + \boldsymbol{e}_i, t + \Delta t) - f_i(\boldsymbol{r}, t) = -\frac{1}{\tau_\rho}[f_i(\boldsymbol{r}, t) - \overline{f_i}(\boldsymbol{r}, t)] + \frac{1}{3}\boldsymbol{F} \cdot \boldsymbol{e}_i. \qquad (4)$$

The second equation describes the interaction of the two fluids:

$$d_i(\boldsymbol{r} + \boldsymbol{e}_i, t + 1) - d_i(\boldsymbol{r}, t) = -\frac{1}{\tau_\Delta}[d_i(\boldsymbol{r}, t) - \overline{d_i}(\boldsymbol{r}, t)], \qquad (5)$$

where $\boldsymbol{F}$ is the body force, f_i and d_i are the distribution functions of the overall density and the density difference respectively, and $\overline{f_i}$ and $\overline{d_i}$ are the corresponding equilibrium distributions. Details of the form of $\boldsymbol{F}$, $\overline{f}_i$ and $\overline{d}_i$ are given in appendix A, as are the macroscopic equation satisfied by such a system. The

units of the lattice are the time-step between collisions and the separation of the grid points: the lattice units (lu).

An important consideration in performing LB simulations is to ensure that the fluid system exhibits Galilean invariance. The LB model becomes non-Galilean invariant when there is a variation in the density, although this can be corrected using a model with a higher number of grid directions [18]. Here variations in ρ occur from two sources: firstly through a small change which occurs at the interface of the binary fluid model (in the absence of gravity) [18], the second is through the density gradient introduced into each fluid by the body force [15]. Here we consider the non-Galilean invariance to be negligible since a density variation of a few percent is likely to produce a similar relative error in the simulation [18]. Further, we note that the density difference between the two binary fluids is influenced by the ratio of the terms g_a and g_b, see appendix A and [15]. However, the variation in the parameter ρ (which leads to Galilean invariance) is influenced by the magnitude of g_a and g_b [15]. This means that any non-Galilean invariance due to the inclusion of gravity will occur over the whole fluid, not just at the interface; however, the vales of g_a and g_b can be selected such that the change in ρ over the whole fluid is negligible but the relative densities of the two fluids, γ, is significant.

2.1 Progressive wave initialisation

The waves were initialised by first setting up a standing wave as described in [4], such that the interface is at an extreme of its oscillation and the fluid velocity is zero everywhere[1]. The standing wave was then allowed to oscillate for a quarter period. The magnitude of the horizontal velocity $\tilde{u}(z)$ is found half way between the node and the antinode, and the magnitude of the vertical velocity $\tilde{w}(z)$ at the antinode. The density profile $\rho(z)$ is found at any value of x. A progressive wave was then initialised with velocities $u(x,z) = \tilde{u}(z)\sin(kx)$ and $w(x,z) = \tilde{w}(z)\cos(kx)$ and density $\rho(x,z) = \rho(z)$. This means that the velocity and density used to initialise the progressive wave simulation are correct for the model and wave parameters selected. The initial values of the distribution functions f_i and d_i are given by $f_i(x,z,t=0) = \overline{f}_i(u(x,z), w(x,z), \rho(z))$ and $d_i(x,z,t=0) = \overline{d}_i(u(x,z), w(x,z), \rho(z))$, where $\overline{f}_i$ and $\overline{d}_i$ are given in appendix A. Finally, the interface $\eta(x) = a\cos(kx)$ is imposed by shifting each column of sites by an amount $\eta(x)$ to produce the interface. Values shifted off the grid are discarded. Sites near the boundary which are not assigned a new value by the shifting operation retain their original value.

[1] This involves insuring that the density profile is correct for the body force which is being imposed. This was achieved in [4] by allowing the system to settle, however, the density profile can also be calculated [15].

3 Wave generation and velocity measurement in a laboratory wave tank

The experiments were performed in a wave flume of length 6m, width 0.4m and total depth 0.6m. To achieve stratification the tank was partially filled with fresh water and then a saline solution was slowly bled in underneath. Using this method a density profile can be set up in the tank which has an approximate tanh profile:

$$\rho = \overline{\rho}\left[1 - \alpha \tanh\left(\frac{2z}{l}\right)\right]. \tag{6}$$

The mean density, $\overline{\rho}$, and the density difference, $2\alpha\overline{\rho}$, are determined by the concentration of the saline solution, while l, which describes the vertical thickness of the interface, was measured using an aspirating conductivity probe. Practically, the thickness of the interface was determined by the length of time over which the saline solution was bled into the tank; this typically took a number of hours. The waves were generated using a friction driven, oscillating paddle, centred about the interface, which was computer controlled and driven in the vertical direction only [5].

3.1 Velocity measurement

The fluid velocity in the tank was measured using Particle Image Velocimetry (PIV) [19, 20, 5, 21]. PIV can be divided into the following stages: seeding,

illumination, image capture, analysis and post processing. The seeding particles used were conifer pollen which have a size of around 70 μm. A measurement area of length 0.5m, centered around 2.6 m from the wavemaker, was illuminated using a 15 W Argon-Ion laser and a scanning beam technique. Figure 1 shows the set up of the tank and laser system. Images of the particles were recorded on 120 format film.

It is a requirement of the analysis technique that the pollen particles must have moved at least two diameters between successive pulses. Due to the slow speed with which internal waves move, this is not always achievable, even for the steep waves being considered here. For this reason an image shifting system [22] was employed which has proved ideal in several studies [23, 24, 25]. The camera photographs the measurement zone through its image in a mirror. The mirror is rotated between exposures and so superimposes an artificial displacement on the actual particle displacement. This displacement is removed after the analysis stage. In the context of the current investigation, image shifting is essential in removing directional ambiguity and minimise effects such as particle overlap [20]. The disadvantage is an effective loss of dynamic range, the absolute dynamic range is the same however the velocities of interest occupy only a fraction of this range, the remainder being occupied by the shift velocity.

PIV analysis is performed by dividing the image of the measurement zone into

several interrogation regions, each containing a number of pollen particle images. The negatives were analysed using a Young's Fringe auto-correlation technique to obtain a velocity vector for each region. The location of symmetric peaks in the two-dimensional auto-correlation plane gives the local mean displacement between successive illumination pulses. Provided the magnitude of the displacement added by the image shifting is greater than the actual displacement, it is also possible to determine in which direction the particles are travelling along the measured displacement. Since the time between the laser pulses is know, the velocity of the particle (including the shifting velocity) can be found. The known shift velocity is then removed during the post-processing. This is not a constant velocity across the whole of the measurement zone [24, 22].

Since PIV analysis is a statistical process, there is a finite probability of an erroneous vector being produced. This can be due to a low seeding concentration in a particular interrogation region, or variations in illumination or visibility. Erroneous vectors, which are very different from the surrounding vectors, can be removed in a region with a poor signal-to-noise ratio. This explains the small number of missing vectors in figures 2 and 4, mainly near the edges of the measurement zone.

Refractive index changes are a potential source of error, however large errors are not realised in practice [26]. In this investigation, the interface region was ap-

proximately mid-way between the top and bottom of the film. Thus the path of the scattered light from the interface region travels approximately normal to the surfaces of the experimental set-up and onto the surface of the recording medium. This greatly reduces refraction effects. Secondly, PIV measures relative displacements. For these wave studies the displacement of the seeding particles is small (hence the need for an image shifting system) and the time separation between frames was significantly shorter than the time for particles to move through the interface. This means that particles which were being correlated were in general in regions of similar refractive index. Finally it should be noted that the interface itself generally consisted of no more than one vector per column.

More recent methods, particularly digital PIV (DPIV) [27, 21, 26], eliminate the need to use image shifting since single particle images are recorded on successive frames rather than multiple exposures on a single image. This eliminates the possibly of the multiple images of a particle overlapping. Furthermore the digital recording of images enables the analysis to be performed using numerical procedures, with cross correlation techniques using Fourier transforms usually employed. Evidently this differs from the Young's fringes method employed here.

4 Comparison between interfacial wave simulations and experimental results

The following comparison is between two interfacial waves: wave_{PIV} which was generated in a wave tank and wave_{LB} which was simulated using the LB model.

4.1 Wave parameters

We now consider the parameters describing the two waves.

4.1.1 Density Profile

Wave_{PIV} has a density profile

$$\rho = \overline{\rho}\left[1 - \alpha \tanh\left(\frac{2z}{l}\right)\right] \tag{7}$$

where $\overline{\rho} = 1044$ kgm^{-3}, $\alpha = 0.044$ and l, the interface thickness, is 0.019m. Away from the interface the asymptotical densities are $\rho_1 = 998$ kgm^{-3} and $\rho_2 = 1090$ kgm^{-3}. The potential density can be considered as being the same as the fluid density here. Wave_{LB} has $\kappa = 0.1$ which gives an interface width with $l \simeq 10$ lattice units (lu). In the upper fluid the density is proportional to g_1 and in the lower fluid it is proportional to g_2. In the interface region we expect the density to vary in a smooth manner since the order parameter varies smoothly over the interface [14]. Away from the interface the ratio of the potential densities is

name	parameter	wave_{PIV}	wave_{LB}	$\frac{\text{wave}_{\text{PIV}}}{\text{wave}_{\text{LB}}}$
Dimensionless interface thickness	l/λ	0.026	9.8×10^{-3}	2.6
Dimensionless wave amplitude	a/λ	0.020	0.017	1.2
Dimensionless upper fluid depth	kh_1	2.1	2.5	0.84
Dimensionless lower fluid depth	kh_2	2.2	3.8	0.58
Density ratio	γ	1.1	1.1	1.0
Froude number (F)	$c\sqrt{k/g'}$	0.99	0.99	1.0
Reynolds number (Re)	$c/(k\nu)$	2.6×10^4	9.2×10^2	28

Table 1: The dimensionless parameters describing wave_{PIV} and wave_{LB}. The depth of the upper and lower fluids are h_1 and h_2 respectively, λ is the wavelength, k is the wavenumber, ν the viscosity, γ is the density ratio of the two fluids, g is the acceleration due to gravity, a is the wave amplitude, c is the wave celerity ω/k, l is the interface thickness and g' is the reduced gravity: $g' = g(\gamma - 1)/(\gamma + 1)$.

$\gamma = \rho_2/\rho_1 = 1.118$ and $\alpha = 0.056$.

4.2 Dimensionless parameters

The parameters describing the two waves are measured in different units. To directly compare the waves it is necessary to consider the dimensionless parameters describing them. There are a number of dimensionless parameters which can be derived, an exhaustive set of independent parameters is shown in table 1. Any other dimensionless parameter can be expressed in terms of these in table 1. For completeness the dimensional parameters are given in appendix B.

4.2.1 Comparison of dimensionless parameters

When comparing two waves, whether they are simulated results, experimental results from a wave tank, results from a field experiment or theoretical predictions, the dimensionless parameters need to be matched as closely as possible. In practice it is not possible to have all the dimensionless parameters the same for both waves but they must be of a similar order. The ratios l/λ are not perfectly matched, but this should only affect the velocities close to the interface. The different interface thicknesses should have little effect on the comparison since the experimental results are measured every 0.0125 m which is similar to l. The ratios a/λ are both of a similar size. The values of kh_i are somewhat different for the two waves, however we are interested in $\tanh(kh_i)$. For both waves this is never smaller than 0.97 in either fluid so both waves can be considered as deep water waves. The values of γ, the density ratio, are similar for both waves giving a density difference of about 10%. The internal Froude number, $F = c\sqrt{k/g'}$, is approximately unity for both waves. This is expected for deep waves through the dispersion relation. The Reynolds number Re, which can be taken to be $c/(k\nu)$, is different for both waves. The Reynolds number of wave_{PIV}, the experimental wave, is almost thirty times the Reynolds number of wave_{LB}, the simulated wave. Both Reynolds numbers are, however, large enough that we expect viscous effects to be small in both waves but slightly larger in the simulated wave. We note that for both waves the value of Re is smaller than would be observed in the

ocean. The effect of the different Reynolds number on the two waves can most easily be seen through the ratio of the boundary layer thickness to the wavelength $\delta/\lambda = \sqrt{Re/(2\pi)}$. Wave_{PIV} and wave_{LB} have $\delta/\lambda = 9.84 \times 10^{-4}$ and 5.24×10^{-3} respectively. Both are small, however the relative boundary layer thickness of the simulated waves is about five times larger. The boundary layer thickness is considerably smaller than the spacing of the experimental results: $\delta/\Delta x \simeq 1/17$, where Δx is the separation of the results. For the simulated waves $\delta/\Delta x = 5.4$ giving several grid points within the boundary layer[2]. It is also interesting to consider δ/l which is 0.037 and 0.534 for wave_{PIV} and wave_{LB} respectively. For both waves this is less than unity, but is larger for wave_{LB} due to its lower Reynolds number.

4.3 Velocity comparisons

The PIV results are shown in figures 2 and 4 at two different times. The simulated results are shown in figures 3 and 5 for areas with the same dimensionless size. The results plotted are the dimensionless velocities, $\boldsymbol{u}/c$. The axes have been chosen so that $z = 0$ is the mean level of the interface and $x = 0$ is at a trough.

Velocity profiles were extracted from the experimental and simulation results

[2]In the presentation of the results here the resolution of wave_{LB} has been reduced in figures 3 and 5 to match the resolution of the experimental results, this gives $\delta/\Delta x = 0.31$.

in figures 2-5. The horizontal profile is shown in figure 6 for the results at the wave trough and in figure 7 at the wave crest. The vertical velocity profile at $x = \lambda/4$, the midpoint between the crest and the trough, is shown in figure 8. The experimental results from figures 2 and 4 are represented by a '$\times$' and a '$+$' respectively. The dashed line represents the simulation results and the solid line is the linear solution (see appendix C). Error bars have been included for a number of the experimental results in figure 6 for an error of $\pm$ 9 %. This is an estimate of the upper bound of the combined errors involved in the measurements calculated away from the interface [28]. The main sources of error in the measurements are: buoyancy of the seeding particles in different density regions; velocity biasing errors in the image analysis, lens aberrations in the image capture system; and refractive index effects. There is clearly some degree of scatter in the experimental results which is generally in agreement with the $\pm$ 9 % error bars. The vertical velocities, displayed in figure 8, show good agreement between the simulation results and the experimental results.

The horizontal results, shown in figures 6 and 7, are qualitatively similar, however quantitatively there are some discrepancies. In each of the three sets of measurements the horizontal velocities in one of the fluids agree well, while in the other fluid the magnitude of the experimental results are somewhat smaller than the simulation results. These discrepancies are too large to be explained by a 9% error in the measurements. As figure 6 demonstrates, it is not always the same

fluid which contains the discrepancy. This effect can also be seen in figures 2 and 4 where the magnitude of the horizontal velocity above and below the troughs and crest are different. Since the difference appears as a shift in the horizontal velocity, it might be suspected that the image-shifting system is introducing the observed difference. This was not the case since any error would be present in both fluids. The distortion and systematic error introduced by the image-shifting system was removed in the PIV post-processing. The biggest difference between the waves is that the wave tank admits an infinite number of vertical modes. The first mode is dominant but other modes may be present. While it is possible that higher modes might develop further over time in the numerical simulation they will be small at the time the measurements were taken since they were not present in the initialisation process. In contrast, higher modes in the laboratory waves may be introduced by the wavemaker. Thus the influence of higher modes will be greater in the PIV results than in the LB simulations. The differences in the dimensionless parameters, see table 1, will undoubtedly contribute to the differences observed in the results. However, it is probable that the main reason for the deviation between the two sets of results is due to the presence of other modes in the experimental results. The presence of higher modes in the experimental results would explain the variations in the horizontal velocities of wave_{PIV} in figure 6. The experimental results were found to satisfy continuity within the error limits.

Despite these differences, the vertical profile is seen to fit well with the experimental results. The horizontal velocity shows the same qualitative features and the comparison is as good as can be expected, given the presence of other modes in the experimental results. It is interesting to note that despite the difference in the Reynolds number there is little difference in the shape of the horizontal velocity close to the interface. The prediction of linear theory is also shown in figures 6, 7 and 8 (solid line) for comparison. The two waves have $ak > 0.1$ so it is not expected that linear theory will provide a good agreement with the steep waves considered here. In each case the results of the simulations predict velocities up to 40% greater than linear theory. The experimental results for the vertical velocities also show higher velocities than linear theory.

5 Conclusion

We have considered the simulation of steep, progressive interfacial internal waves using a LB model and the measurement of the velocity field of a steep, progressive interfacial wave in a wave tank using PIV. A comparison has been made between the simulated waves and experimental waves. The results were seen to be in qualitative agreement. Quantitative differences are believed to be due to the rather unsteady nature of the steep wave group as it propagates in the laboratory tank and the presence of higher modes.

6 Acknowledgements

This work was partially funded by the UK Health and Safety Executive through the Marine Technology Support Unit and by EPSRC (UK).

References

[1] A. Osborne, T. Burch, and R. Scarlet. The influence of internal waves on deep water drilling. *J. Petroleum Tech.*, pages 1497–1503, 1978.

[2] J. B. Bole, C. C. Ebbesmeyer, and R. B. Romea. Soliton currents in the south china sea: Measurements and theoretical modelling (OTC 7417). In *Proceedings of the 26th Annual Ocean Technology Conference*, pages 2–5, 1994.

[3] T. J. Sherwin. Evidence of a deep internal tide in the Faeroe-Shetland channel. In Tidal Hydrodynamics, editor, *B. B. Parker*, pages 469–488. Wiley, New York, 1991.

[4] J. M. Buick and C. A. Greated. Lattice boltzmann modeling of interfacial gravity waves. *Physics of Fluids*, 10:1490–1511, 1998.

[5] A. J. Martin and W. J. Easson. Non-linear internal wave kinematics. In *Proceedings of the seventh International Offshore and Polar Engineering, ConferenceISOPE 97*, volume 3, pages 122–129, Honolulu, USA, 1997.

[6] J. Grue, A. Jensen, P. O. Rusas, and J. K. Sveen. Breaking and broadening of internal solitary waves. *J. Fluid Mech.*, 413:181–217, 2000.

[7] M. La Rocca, G. Sciortino, and M. A. Boniforti. Interfacial gravity waves in a two-fluid system. *Fluid Dynamics Research*, 30:31–63, 2002.

[8] R. E. L. Turner and J.-M. Vanden-Broeck. The limiting configuration of interfacial gravity waves. *Phys. Fluids*, 29:372–375, 1986.

[9] A. P. Stamp and M. Jacka. Deep-water internal solitary waves. *J. Fluid Mech.*, 305:347–371, 1995.

[10] D. E. Terez and O. M. Knio. Numerical simulations of large-amplitude internal solitary waves. *J. Fluid Mech.*, 362:53–82, 1998.

[11] Y. H. Qian, D. d' Humières, and P Lallemand. Lattice BGK models for Navier-Stokes equation. *Europhysics Letters*, 17 (6):479–484, 1992.

[12] S. Chen G. D. Doolen. Lattice Boltzmann method for fluid flows. *Annu. Rev. Fluid Mech.*, 30:329–364, 1998.

[13] E. Orlandini, M. R. Swift, and J. M. Yeomans. A lattice Boltzmann model of binary-fluid mixtures. *Europhysics Letters*, 32 (6):463–468, 1995.

[14] M. R. Swift, E. Orlandini, W. R. Osborn, and J. M. Yeomans. Lattice Boltzmann simulation of liquid-gas and binary fluid systems. *Physical Review E*, 54 (5):5041–5052, 1996.

[15] J. M. Buick and C. A. Greated. Gravity in a lattice Boltzmann model. *Phys. Rev. E*, 61:5307–5320, 2000.

[16] J. Buick, W. Easson, and C. Greated. Simulation of wave motion using a lattice gas model. *Int. J. Numer. Meth. Fluids*, 22:313–321, 1996.

[17] J. M. Buick, C. A. Greated, and W. J. Easson. Investigation of a lattice gas model for surface gravity waves. *Physics of Fluids*, 9:2585–2597, 1997.

[18] K. Langaas and J. M. Yeomans. Lattice Boltzmann simulation of a binary fluid with different phase viscosities and its application to fingering in two dimensions. *European Physical Journal B*, 15:133–141, 2000.

[19] R.J. Adrian. Particle-imaging techniques for experimental fluid mechanics. *Ann. Rev. Fluid Mech.*, 23:261–304, 1991.

[20] M. Raffel, C. Willert, and J. Kompenhans. *Particle Image Velocimetry: a practical guide*. Springer, Heidelberg, 1998.

[21] X. Ni, J. A. Cosgrove, A. D. Arnott, C. A. Greated, and R. H. Cumming. On the measurement of strain rate in an oscillatory baffled column using particle image velocimetry. *Chem. Eng. J.*, 55:3195–3208, 2000.

[22] M. Raffel and J. Kompenhans. Theoretical and experimental aspects of image-shifting by means of a rotating mirror system for particle image velocimetry. *Meas. Sci. Tech.*, 6:795–805, 1995.

[23] C. Gray, C. A. Greated, D. R. McCluskey, and W. J. Easson. An analysis of the scanning beam PIV illumination system. *Measurement Science and Technology*, 2:717–724, 1991.

[24] I. G. Morrison. *The Hydrodynamic Performance of an Oscillating Water Column Wave Energy Converter*. PhD thesis, The University of Edinburgh, 1995.

[25] N. Emarat. *Particle image velocimetry experiments on surf-zone breaking waves*. PhD thesis, The University of Edinburgh, 2000.

[26] A. E. Thomas. *The interaction of an internal solitary wave with suface gravity waves*. PhD thesis, The University of Edinburgh, 2002.

[27] J. Westerweel. Fundamentals of digital particle image velocimetry. *Measurement Science and Technology*, 8:1379–1392, 1997.

[28] A. J. Martin. *Laboratory Simulation and numerical modelling of the kinematics of oceanic internal waves*. PhD thesis, The University of Edinburgh, 1997.

[29] S. A. Thorpe. On the shape of progressive internal waves. *Philosophical Transactions of the Royal Society A*, 263:563–614, 1968.

[30] Nag. Routine D02KEF. The NAG Fortran Library, Mark 14, 1990.

A Details of the binary fluid model

The parameters $\boldsymbol{F}$, $\overline{f_i}$ and $\overline{d_i}$ are given by [15, 13, 14]

$$\boldsymbol{F} = \rho g = g_a(\rho - \Delta\rho) + g_b(\rho + \Delta\rho)\boldsymbol{k}, \tag{8}$$

$$\overline{f}_i = A + Bu_\alpha e_{i\alpha} + Cu^2 + Du_\alpha u_\beta e_{i\alpha} e_{i\beta} + G_{\alpha\beta} e_{i\alpha} e_{i\beta}, \quad i = 1, ..., 6, \tag{9}$$

$$\overline{f}_0 = A_0 + C_0, \tag{10}$$

$$\overline{d}_i = H + Ku_\alpha e_{i\alpha} + Ju^2 + Qu_\alpha u_\beta e_{i\alpha} e_{i\beta}, \quad i = 1, ..., 6 \tag{11}$$

and

$$\overline{d}_0 = H_0 + J_0, \tag{12}$$

where summation over the repeated indices α and β is assumed and

$$A_0 = \rho - 6A, \quad A = (\rho T - \kappa\Delta\rho\nabla^2\Delta\rho/2 - \kappa\rho\nabla^2\rho/2)/3, \quad B = \rho/3, \quad C = -\rho/6,$$

$$C_0 = -\rho, \quad D = 2\rho/3, \quad G_{xy} = G_{yx} = \frac{2\kappa}{3}\left[\frac{\partial\rho}{\partial x}\frac{\partial\rho}{\partial y} + \frac{\partial\Delta\rho}{\partial x}\frac{\partial\Delta\rho}{\partial y}\right], \quad H_0 = \Delta\rho - 6H,$$

$$G_{xx} = -G_{yy} = \frac{\kappa}{3}\left[\left(\frac{\partial\rho}{\partial x}\right)^2 - \left(\frac{\partial\rho}{\partial y}\right)^2 + \left(\frac{\partial\Delta\rho}{\partial x}\right)^2 - \left(\frac{\partial\Delta\rho}{\partial y}\right)^2\right],$$

$$H = \Gamma\Delta\mu/3, \quad K = \Delta\rho/3, \quad J = -\Delta\rho/6, \quad J_0 = -\Delta\rho, \quad Q = 2\Delta\rho/3. \tag{13}$$

The chemical potential difference is given by

$$\Delta\mu = -\frac{\Lambda}{2}\frac{\Delta\rho}{\rho} + \frac{T}{2}\log\left(\frac{1+\Delta\rho/\rho}{1-\Delta\rho/\rho}\right) - \kappa\nabla^2\Delta\rho. \tag{14}$$

The interfacial energy κ, the temperature T, the interaction strength parameter Λ, the mobility Γ and the relaxation times τ_ρ and τ_Δ (in equations (4) and (5)) are free to be varied to change the properties of the binary fluid. Here these parameters have the values $\kappa = 0.001$, $T = 0.5$, $\Lambda = 1.1$, $\Gamma = 0.1$ and $\tau_\Delta = 0.789$. The relaxation parameter for the whole fluid determines the viscosity of the fluid as

$$\nu = \frac{2\tau_\rho - 1}{8}. \tag{15}$$

With this selection of parameters $g_1 \simeq 3g_a/4 + g_b/4$ and $g_2 \simeq g_a/4 + 3g_b/4$.

The macroscopic equations for the binary fluid system can be found using a Taylor expansion technique [14, 18, 15] to give, in the incompressible limit, the continuity equation

$$\frac{\partial\rho}{\partial t} + \nabla\cdot\rho\boldsymbol{u} = 0; \tag{16}$$

the Navier-Stokes equation

$$\frac{\partial(\rho\boldsymbol{u})}{\partial t} + (\nabla\cdot\rho\boldsymbol{u})\boldsymbol{u} = -\nabla p_0 + \nu\nabla^2(\rho u_\alpha) + \nabla\left[\zeta\nabla\cdot(\rho\boldsymbol{u})\right] + \boldsymbol{F}, \tag{17}$$

where ν and ζ are the kinematic and bulk viscosities and p_0 is the pressure; and the convection-diffusion equation

$$\frac{\partial \Delta\rho}{\partial t} + \nabla(\Delta\rho \boldsymbol{u}) = \Gamma\theta\nabla^2\Delta\mu + Z, \tag{18}$$

where θ is the diffusion coefficient and Z can be neglected [18].

B Dimensional parameters

The wave parameters for the two waves and the units they are measured in are shown in table 2.

	wave_{PIV}		wave_{LB}	
parameter	value	unit	value	unit
h_1	0.245	m	414	lu
h_2	0.254	m	610	lu
λ	0.740	m	1024	lu
k	8.49	m^{-1}	6.14×10^{-3}	lu^{-1}
ω	1.9	s^{-1}	1.73×10^{-3}	$(\text{time-steps})^{-1}$
ν	1.0×10^{-6}	$\text{m}^2 s^{-1}$	0.05	$\text{lu}^2(\text{time-steps})^{-1}$
δ	7.3×10^{-4}	m	5.37	lu
g	9.8	ms^{-1}	9.0×10^{-3}	lu $(\text{time-steps})^{-1}$
a	0.015	m	17.3	lu
c	0.22	ms^{-1}	0.282	lu $(\text{time-steps})^{-1}$
l	0.019	m	10	lu

Table 2: The value of the parameters describing wave_{PIV} and wave_{LB} and the units in which they are measured. The depth of the upper and lower fluids are h_1 and h_2 respectively, λ is the wavelength, k is the wavenumber, ω the frequency, ν the viscosity, δ is the boundary layer thickness $(\nu/\omega)^{1/2}$, g is the acceleration due to gravity, a is the wave amplitude, c is the wave celerity ω/k, and l is the interface thickness.

C First-order analytic solution

Based on the analysis of Thorpe [29], it can be shown that the streamfunction ψ, defined such that $u = -\psi_z$ and $w = \psi_x$, satisfies the vorticity equation [5, 28]

$$\nabla^2\psi_{tt} - \frac{g\rho_z}{\rho+\tilde{\rho}}\psi_{xx} = Q_v + Q_b + Q_d + Q_\nu, \tag{19}$$

where

$$\begin{aligned}
Q_v &= J(\nabla^2\psi, \psi)_t, \\
Q_b &= -\frac{g}{\rho+\tilde{\rho}} J(\tilde{\rho}, \psi)_x, \\
Q_d &= \frac{1}{\rho+\tilde{\rho}} \{\tilde{\rho}_t \left[J(\nabla^2\psi, \psi) - \nabla\psi_t\right] \\
&\quad + (\tilde{\rho}_x \left[J(\psi_x, \psi) - \psi_{xt}\right] + (\rho+\tilde{\rho})_z \left[J(\psi_z, \psi) - \psi_{zt}\right])_t\}, \\
Q_\nu &\simeq \nu(\nabla^2\psi_{xx} - \nabla^2\psi_{zz})_t,
\end{aligned} \tag{20}$$

and the subscripts represent differentiation, g is the acceleration due to gravity, $\rho(z)$ is the static density profile, $\tilde{\rho}(x,z,t)$ is the small density fluctuations due to the wave motion, J is the Jacobian derivative: $J(a,b) = b_z a_x - b_x a_z$ and Q_v, Q_b, Q_d and Q_ν represent non-linear terms. Here Q_v contains terms which are neglected when the Navier-Stokes equation is linearised; Q_b contains non-linear terms which arise from the buoyancy equation; Q_d contains terms which are neglected in the Boussinesq approximation; and Q_ν contains the viscous terms. Assuming that Q_ν can be neglected, solutions for equation (19) can be obtained

[5, 28] by means of a perturbation expansion in $\epsilon = ak$ following Thorpe [29]:

$$\psi(x,z,t) = \epsilon\Psi^{(1)}(z)e^{i(kx-\omega t)} + \epsilon^2\Psi^{(2)}(z)e^{2i(kx-\omega t)} + ... \tag{21}$$

To first order this gives [5, 28]

$$\Psi^{(1)}_{zz} + \frac{\rho_z}{\rho}\Psi^{(1)}_z + \left(\frac{g\rho_z}{c^2\rho} + k^2\right)\Psi^{(1)} = 0. \tag{22}$$

Note that this reduces to Thorpe's equation [29] if we make the Boussinesq approximation, an approximation which can be made in the ocean. In the wave tank and simulations the Boussinesq approximation is satisfactory for the first order expansion considered here, however, it could not be applied in a higher order theory. Equation (22) can be solved with the bottom boundary condition $\psi(x, z_{\text{bottom}}, t) = 0$ and the 'rigid lid' surface condition $\psi(x, z_{\text{surface}}, t) = 0$ using a 'shooting method' [30].

Figure Captions

Figure 1: A schematic diagram of the wave tank and laser system.

Figure 2: Vector plot of the dimensionless velocity $\boldsymbol{u}/c$ for wave_{PIV} at time 1.

Figure 3: Vector plot of the dimensionless velocity $\boldsymbol{u}/c$ for wave_{LB} corresponding to wave_{PIV} in figure 2.

Figure 4: Vector plot of the dimensionless velocity $\boldsymbol{u}/c$ for wave_{PIV} at time 2.

Figure 5: Vector plot of the dimensionless velocity $\boldsymbol{u}/c$ for wave_{LB} corresponding to wave_{PIV} in figure 4.

Figure 6: The horizontal component of the dimensionless velocity $u' = u/c$ as a function of the dimensionless length z/λ for the two troughs shown in figure 2 ($\times$) and figure 4 ($+$). The dashed line represents the simulation results. Also shown, for comparison, is the linear solution (solid line), see appendix C.

Figure 7: The horizontal component of the dimensionless velocity $u' = u/c$ as a function of the dimensionless length z/λ for the crest shown in figure 4 ($+$). The dashed line represents the simulation results. Also shown, for comparison, is the linear solution (solid line), see appendix C.

Figure 8: The vertical component of the dimensionless velocity $w' = w/c$ as a function of the dimensionless length z/λ at $x = \lambda/4$ shown in figure 2 ($\times$) and figure 4 ($+$). The dashed line represents the simulation results. Also shown, for comparison, is the linear solution (solid line), see appendix C.

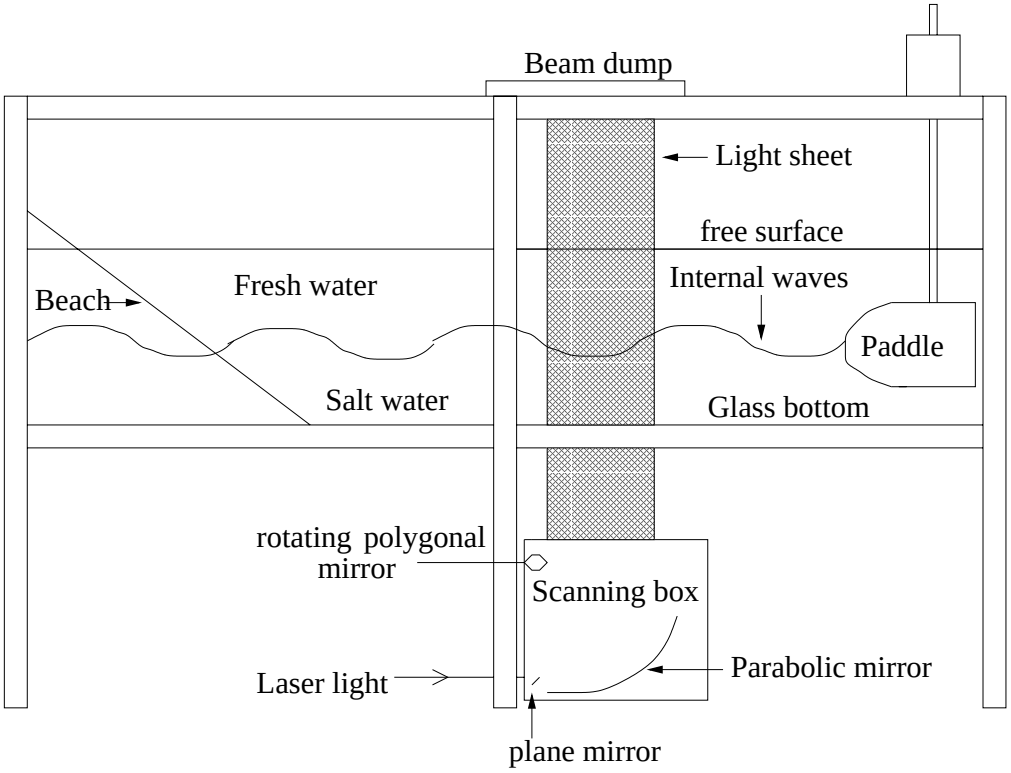

Buick Figure 1.

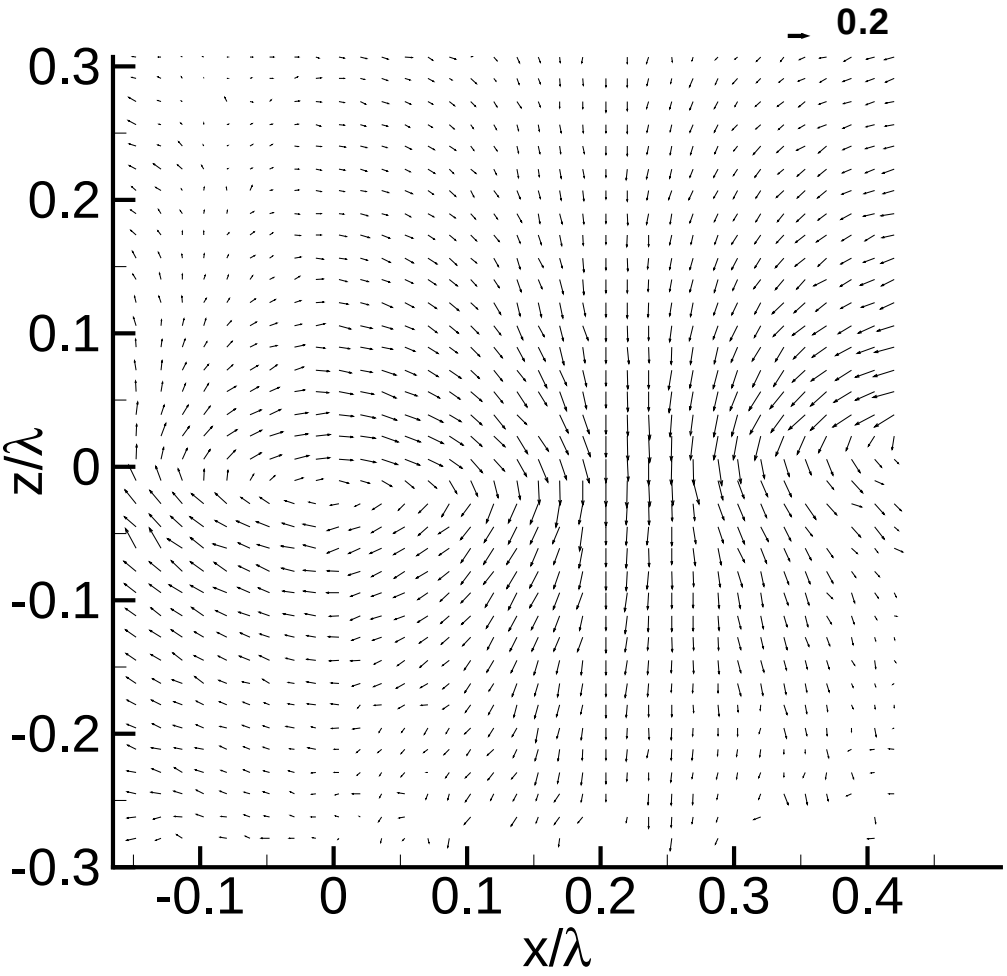

Buick Figure 2.

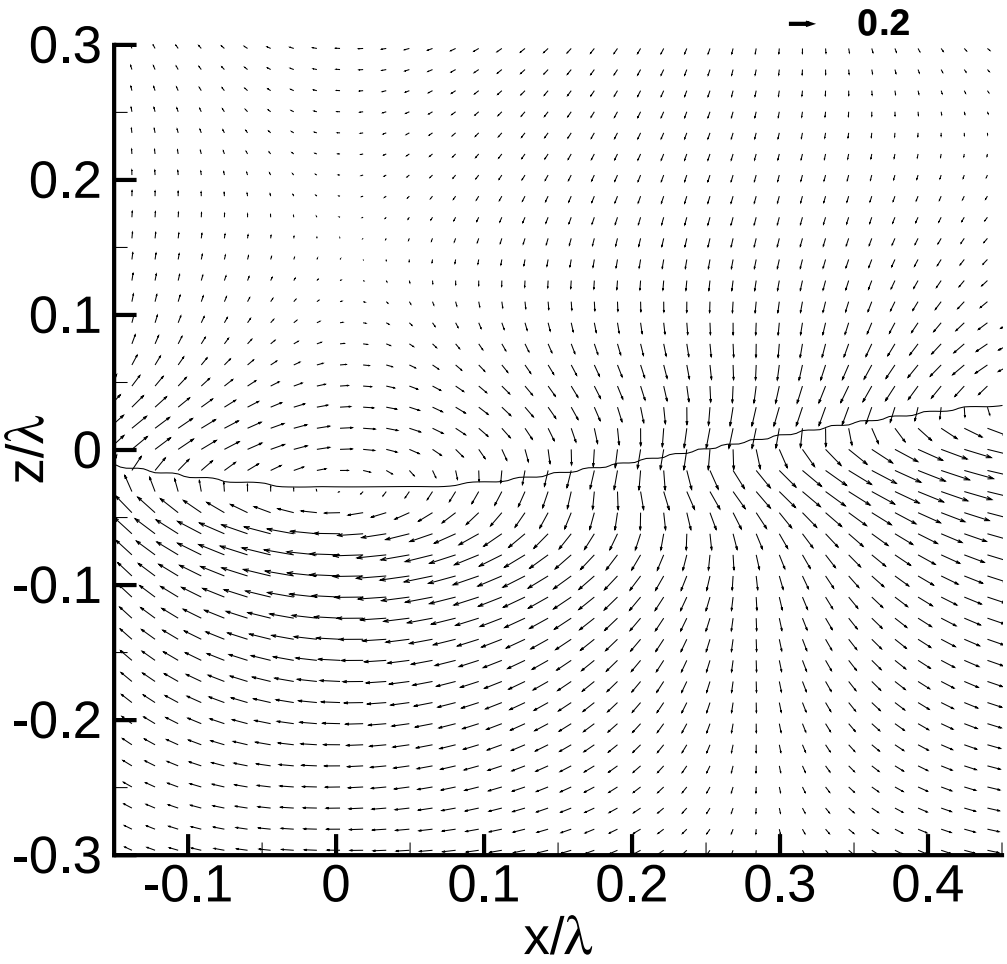

Buick Figure 3.

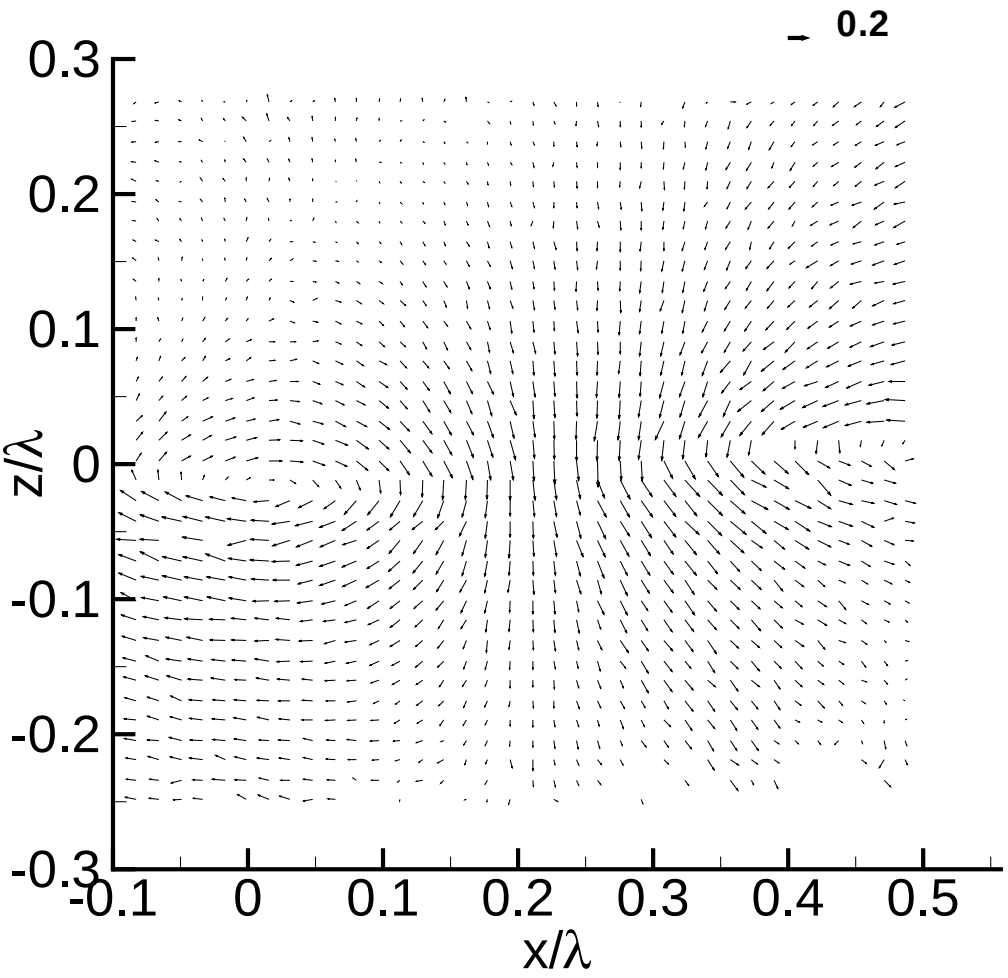

Buick Figure 4.

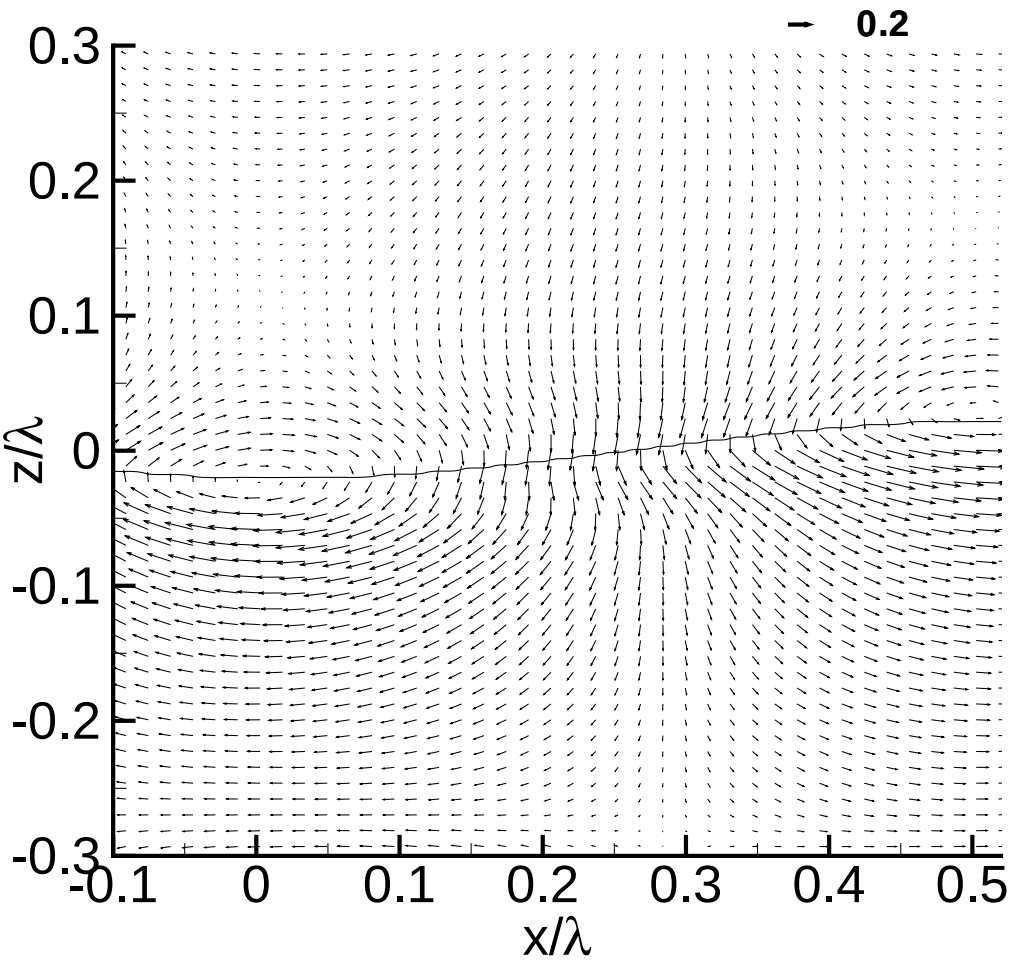

Buick Figure 5.

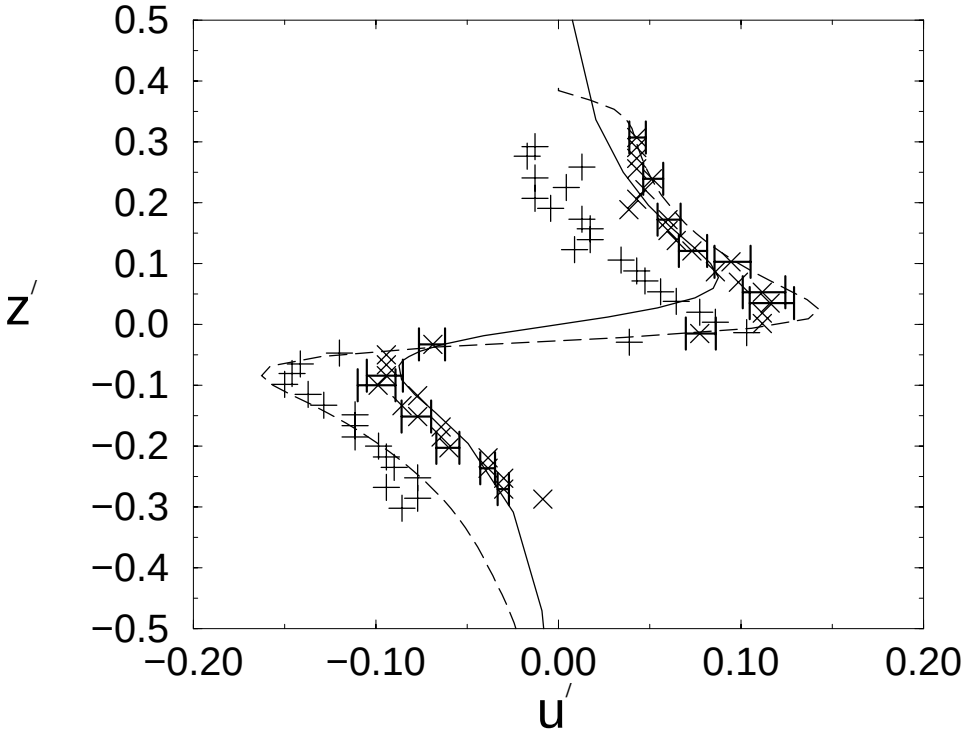

Buick Figure 6.

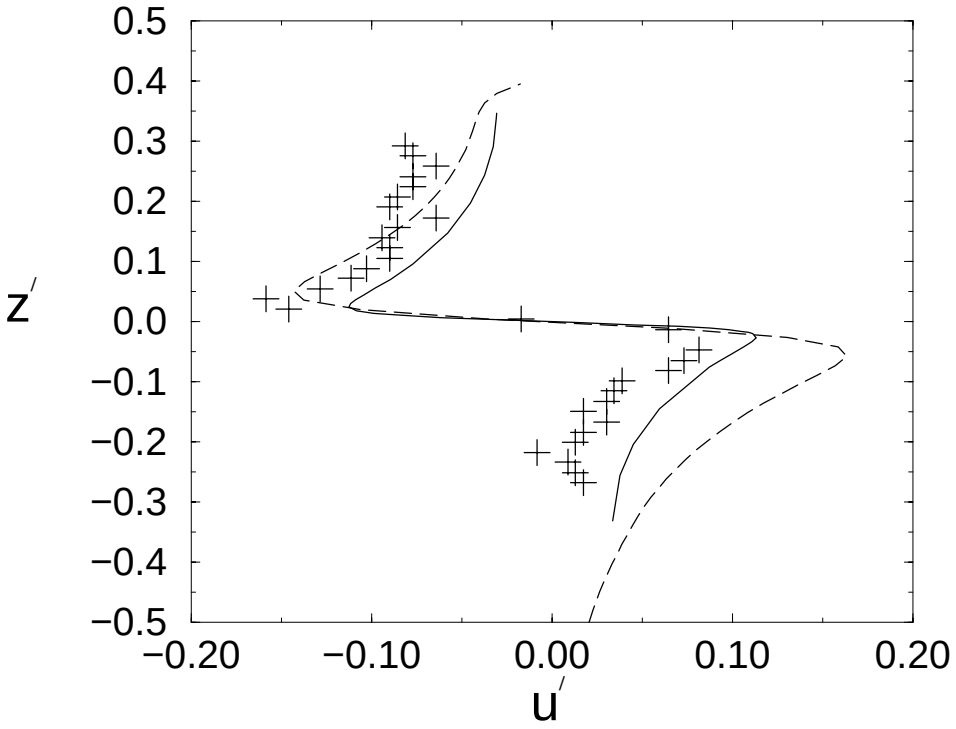

Buick Figure 7.

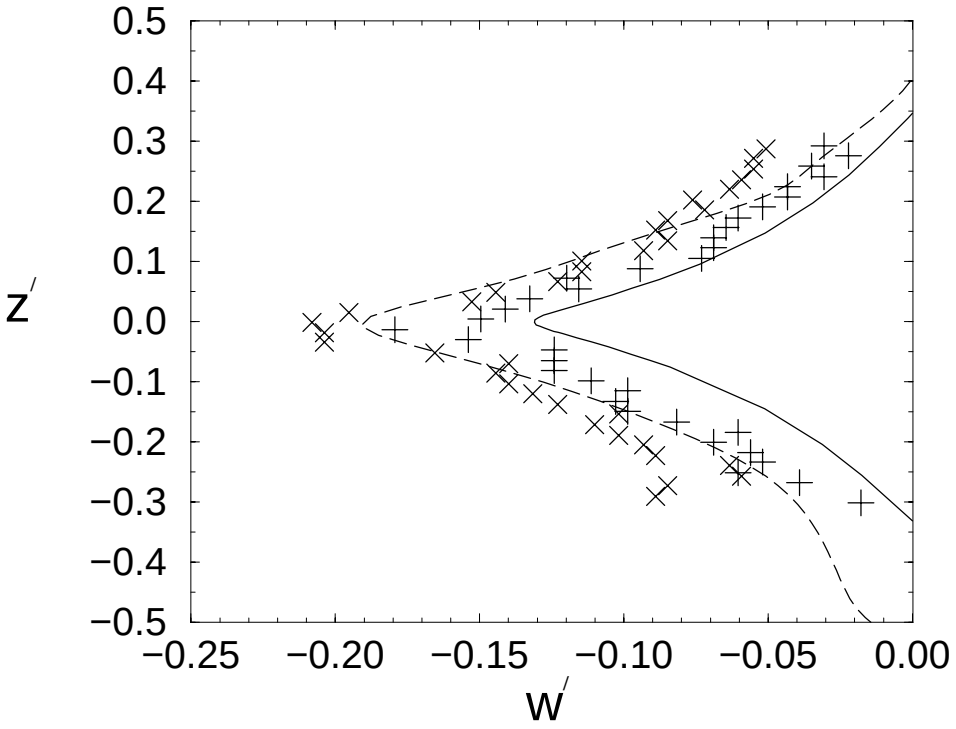

Buick Figure 8.